Acta Oceanol. Sin., 2016, Vol. 35, No. 5, P. 24–37
DOI: 10.1007/s13131-016-0859-0
http://www.hyxb.org.cn
E-mail: hyxbe@263.net

Interdecadal change of winter SST variability in the Kuroshio Extension region and its linkage with Aleutian atmospheric low pressure system

YU Peilong[1], ZHANG Lifeng[1]*, ZHANG Yongchui[1], DENG Bing[2]
[1] College of Meteorology and Oceanography, PLA University of Science and Technology, Nanjing 211101, China
[2] Beijing Institute of Applied Meteorology, Beijing 100029, China

Received 28 September 2015; accepted 20 January 2016

Abstract

By utilizing multiple datasets from various sources available for the last 100 years, the existence for the interdecadal change of the winter sea surface temperature (SST) variability in the Kuroshio Extension (KE) region is investigated. And its linkage with the Aleutian Low (AL) activity changes is also discussed. The results find that the KE SST variability exhibits the significant ~6 a and ~10 a oscillations with obvious interdecadal change. The ~6 a oscillation is mainly detected during 1930–1950, which is largely impacted by the anomalous surface heat flux forcing and Ekman heat transport associated with the AL intensity variation. The ~10 a oscillation is most evident after the 1980s, which is predominantly triggered by the AL north-south shift through the bridge of oceanic Rossby waves.

Key words: sea surface temperature (SST) variability, interdecadal change, Kuroshio Extension, Aleutain Low

Citation: Yu Peilong, Zhang Lifeng, Zhang Yongchui, Deng Bing. 2016. Interdecadal change of winter SST variability in the Kuroshio Extension region and its linkage with Aleutian atmospheric low pressure system. Acta Oceanologica Sinica, 35(5): 24–37, doi: 10.1007/s13131-016-0859-0

1 Introduction

The Kuroshio Extension (KE) is an eastward inertial jet as the Kuroshio leaving the east coast of Japan. The warm water transported by the Kuroshio from the low-latitude ocean makes the KE provide a large quantity of heat to the North Pacific atmosphere, especially in winter (Liu et al., 2006; Wang et al., 2015). This heat release is important for maintaining the surface baroclinicity, anchoring, and energizing the overlying storm track (Kelly et al., 2010). In this region, sea surface temperature (SST) anomaly plays the primary role in determining the profound changes in surface turbulent heat flux (Tanimoto et al., 2003). Accordingly, via modifications in the surface heat release, the KE SST anomaly may have a significant impact on the storm track and then cause the obvious variation of atmospheric circulation. Numerical experiments also indicate that the large-scale atmospheric circulation response is more sensitive to the SST anomaly in the KE region compared with that in other regions of extratropical basins due to the proximity to the storm track (Peng and Whitaker, 1999).

Given its importance in the North Pacific ocean-atmosphere interaction and climate, the KE SST variability and its relevant mechanism deserve to be studied. It has been found that the KE SST anomaly is mainly controlled by the modulations of its dynamic state (Qiu, 2000; Vivier et al., 2002). A warm (cold) KE SST anomaly tends to be induced by a northward (southward) path shift and an intensified (weakened) penetration of the KE jet when it is in a stable (an unstable) state, indicating that ocean circulation variability has a substantial impact on the modification of thermal balance in the KE region. Based on observational data and numerical simulations, many studies have reached a consensus that the KE dynamic state is forced by the wind-driven Rossby waves (e.g., Qiu, 2003; Qiu and Chen, 2005, 2010). Specifically, when the central North Pacific wind stress curl (WSC) anomalies are positive, the negative sea surface height (SSH) anomalies are generated by the enhanced Ekman divergence. These wind-induced SSH signals propagate westward and reach the KE region after a delay of a few years, which leads to an unstable KE dynamic state with a cooling tendency in SST. The sequent reverse occurs when the anomalous WSC forcing is negative in the central North Pacific. This westward propagation process across the North Pacific basin is essential for bringing about a decadal time scale in the KE SST variability (Kwon and Deser, 2007; Qiu et al., 2007).

The WSC fluctuations in the North Pacific are mainly modulated by the Aleutian Low (AL) activity changes (Ishi and Hanawa, 2005), indicating that these AL variations seem to be related to the ~10 a KE SST variability. This hypothesis has been verified by Sugimoto and Hanawa (2009). In fact, as a dominant atmospheric system in the North Pacific, the AL has the significant long-term variations (Trenberth, 1990; Trenberth and Hurrell, 1994), which are the major cause of the SST variability therein on the interannual and longer time scales (Latif and Barnett, 1994, 1996; Overland et al., 1999). However, a remarkable climate transition occurred in the late 1970s in the North Pacific (Trenberth, 1990; Miller et al., 1994). This raises a question that whether the KE SST variability is different before and after

---

Foundation item: The National Basic Research Program (973 program) of China under contract No. 2013CB956203; the National Natural Science Foundation of China under contract No. 41375063.

*Corresponding author, E-mail: zhanglif_qxxy@sina.cn

the transition, and is this non-stationarity also manifested in the AL activity changes? Therefore, the purpose of this study is to investigate the potential interdecadal change of KE SST variability and its linkage with the AL activity changes by using the multiple datasets from various sources available for the last 100 years (1910–2009).

The remainder of this paper is organized as follows. Section 2 describes the datasets and methods used in this study. The century-long KE SST variability and AL activity changes are explored in Sections 3 and 4, respectively. The impacts of AL activity on the interdecadal change of KE SST variability are examined in Section 5. Conclusions are given in Section 6.

2 Data and methods

2.1 *Data*

Seven different SST datasets are used to assess the KE SST variability since 1910: National Oceanic and Atmospheric Administration Extended Reconstructed SST version 3 (ERSSTv3b; Smith et al., 2008); Hadley Centre Sea Ice and SST version 1 (HadISST1; Rayner et al., 2003); Kaplan Extended SST version 2 (Kaplanv2; Kaplan et al., 1998); Simple Ocean Data Assimilation (SODA) SST product (Giese and Ray, 2011); Minobe and Maeda (2005); Hadley Centre SST version 2 (HadSST2; Rayner et al., 2006) and 3 (HadSST3; Kennedy et al., 2011a; Kennedy et al., 2011b). ERSSTv3b (2°×2°), HadISST1 (1°×1°), Kaplanv2 (5°×5°), and SODA (0.5°×0.5°) are "analyzed" products which are optimally interpolated and smoothed in both time and space with different procedures. Minobe SST (1°×1°), HadSST2 and 3 (5°×5°) are "unanalyzed" products (e.g., without smoothing or interpolation) and differ in quality-control and bias correction procedures. More notable is that HadSST3, as a new product published by the Met Office Hadley Centre, is adjusted to reduce the bias from the changes in instrumentation and data availability and consists of 100 interchangeable ensemble members capturing the estimated uncertainties. Therefore, combined with other products, the usage of HadSST3 means that there are in fact 106 SST datasets employed in this study.

To avoid the impact of inadequate SST data coverage existed in the early 20th century, we still use the surface air temperature from Hadley Centre/Climate Research Unit Temperature version 3 (HadCRUT3; Brohan et al., 2006). HadCRUT3 (5°×5°) is also "unanalyzed" product like HadSST2, but the two datasets are actually independent measured based on different observational platforms or instruments (Deser et al., 2010). Thus, HadCRUT3 provides a validation for the results obtained by SST datasets. Numerous studies have used these above datasets to study long-term local or global SST variation and its relation with other variables (e.g., Deser et al., 2010; Zhang et al., 2010; Jin and Wang, 2011; Wu et al., 2012; Li et al., 2013).

In addition, some atmospheric and oceanic variables are also adopted. The net surface heat flux, sea level pressure (SLP), and surface wind stress fields are derived from the ensemble mean fields of Twentieth-Century Reanalysis dataset version 2 (20CRv2; Compo et al., 2011), which assimilates the synoptic surface pressure observations and prescribes monthly SST and sea ice distributions as boundary conditions for the atmosphere. The SSH field is taken from the SODA reanalysis product (Carton and Giese, 2008), which is created by assimilating timely temperature and salinity observational profiles based on the Parallel Ocean Program ocean model. The year-to-year transport of the Kuroshio Current derived from repeat hydrographic surveys is in good agreement with that calculated from SODA, indicating that SODA can reasonably reproduce the variability of the Kuroshio Current (Wu et al., 2012).

A widely used index for long-term climate variability in the North Pacific, namely, the Pacific Decadal Oscillation (PDO) index, is compared with variability of the KE SST and the AL activity. The monthly PDO index (PDOI) is defined by Mantua et al. (1997) and is available online at http://jisao.washington.edu/pdo/PDO.latest.

2.2 *Methods of analysis*

Wavelet spectrum analysis (Torrence and Compo, 1998) is applied to depict detailed features about variability of the KE SST and the AL activity and their dominant relationships on different time scales. Linear correlation and regression analysis are also used. All time series or fields are linearly detrended before further calculation. Statistical significances of correlation or regression coefficients are assessed by two-tailed student's *t*-test using an effective temporal degree of freedom, which takes the serial-autocorrelation into consideration (Trenberth, 1984; Bretherton et al., 1999).

In our present study, the winter season (January-March, hereafter JFM) when the most intense air-sea interaction occurs is considered. All anomalies of variables are calculated relative to the 1961–1990 mean, consistent with HadCRUT3, HadSST2 and 3.

3 Variability of the KE SST

Following Qiu et al. (2007), an index defined as the SST anomalies averaged in the KE region (32°–38°N, 142°–180°E) is used to depict the KE SST variability. Figure 1a shows the time series of KE SST indices computed from various datasets. It can be found in Figs 1a and b that the differences among these datasets are most evident prior to 1916 and during 1940–1950. The large un-

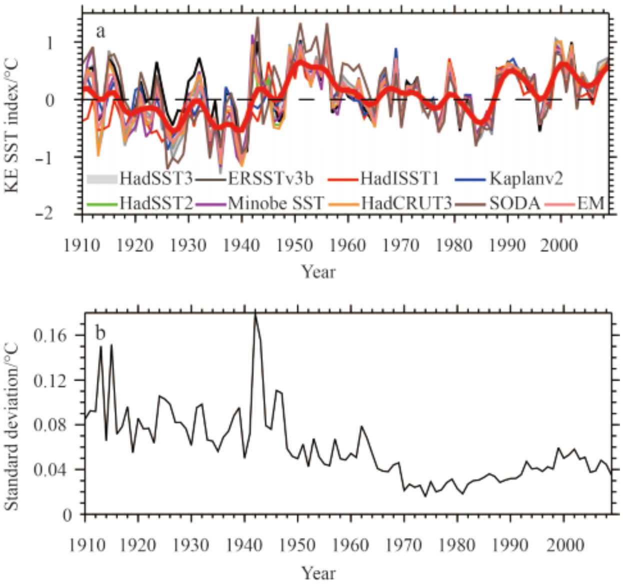

Fig. 1. Time series of the wintertime (JFM) KE SST indices for various datasets and their ensemble mean (EM) over the 1910–2009 period. Red thick line denotes the interdecadal component (> 8 a) of EM derived by the Gaussian filter (a), and time series of the uncertainties (b) determined by one standard deviation among different datasets in (a).

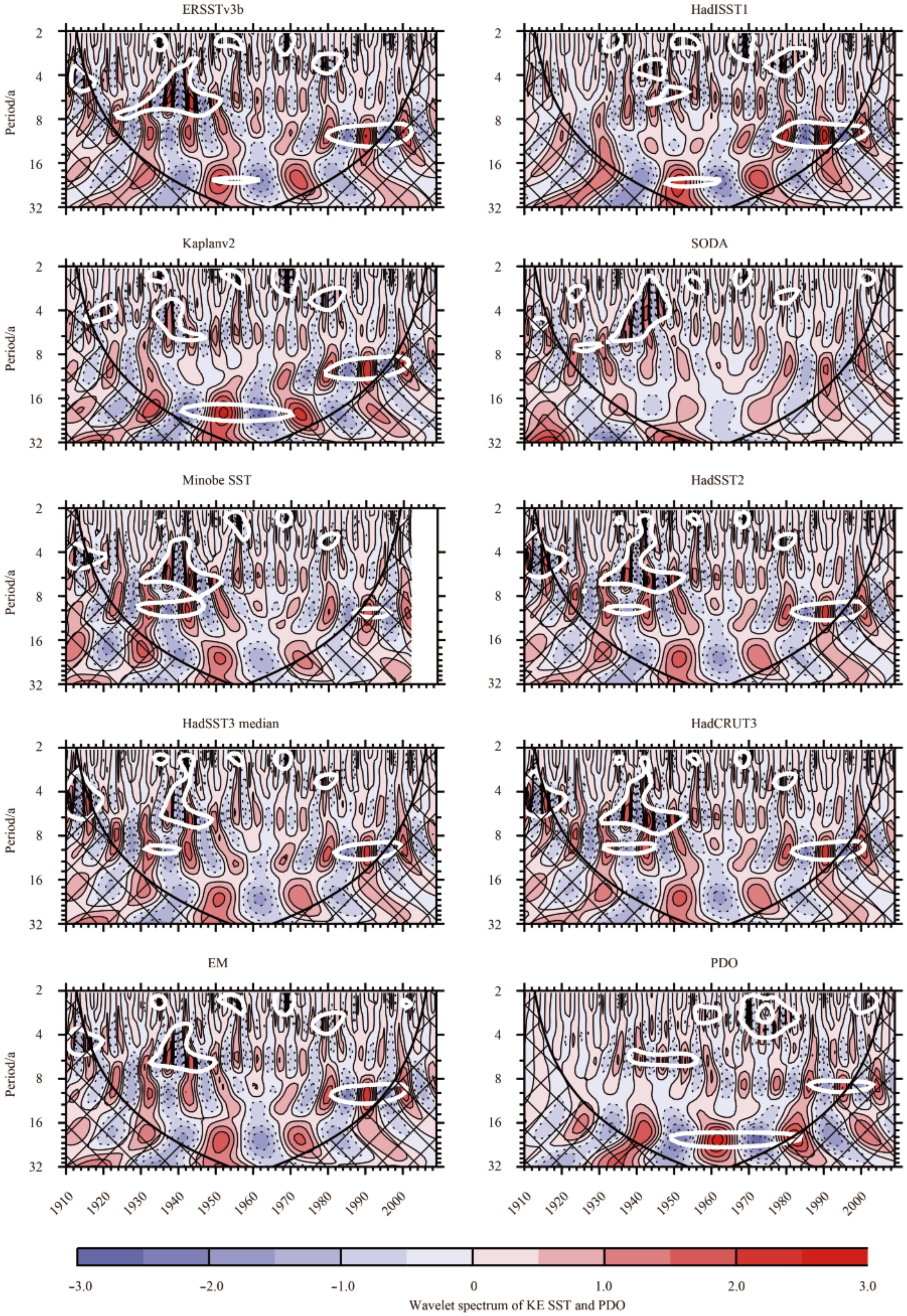

Fig. 2. Morlet wavelet transform coefficients for normalized time series of the KE SST indices (including their EM) in Fig. 1 and the PDO index. The hatched regions indicate the "cone-of-influence" where edge effects may distort the result. White thick contours designate the 90% confidence level against red noise.

certainties in the two subperiods may be resulted from worse data coverage and different analysis methods used in the reconstructions (Kennedy et al., 2011a, 2011b). Despite these discrepancies, all datasets show the two features of KE SST variability consistently from the visual inspection. First, the obvious variation of warm-cold-warm signals on interannual-to-interdecadal time scales is found. Second, the cooling trend during 1910–1940 and 1952–1985 but the warming trend during 1941–1951 and 1986–2009 are exhibited.

In order to get a further understanding of the KE SST variability, a wavelet analysis is performed. Figure 2 shows the results of KE SST indices for various datasets in Fig. 1. Interestingly, it is found that the dominant time scale in KE SST varies unstably in time domain. To be specific, all datasets indicate that the ~6 a oscillation with large amplitudes appears on the time scale of ~6 a (about 5–7 years) during 1930–1950, despite large uncertainties existed in this subperiod (see Fig. 1). However, it becomes weaker with time and is gradually overtaken by the ~10 a (about 9-11 years) one after the 1980s. The ~10 a oscillation has been reported by Qiu et al. (2007) and Sugimoto and Hanawa (1989), but the ~6 a one was not addressed in previous studies. The consistency among different datasets suggests that it is robust for this interdecadal change of KE SST variability.

Although the significances of ~6 or ~10 a oscillation are dataset-dependent, the ensemble mean (EM) of these datasets shows that both of the oscillations are conspicuous. The EM can obtain the commonality among different datasets effectively and reflect the KE SST variability objectively. Therefore, we defined it as the merged KE SST index (MKESSTI) in the following. However, we can not merge the SST field directly by using the similar ways to merge the KE SST index owing to the different resolution of datasets and the interpolation may also bring distinct errors in the "unanalyzed" datasets when the inadequate data coverage appears. Henceforth, the SST field used hereafter is only derived from ERSSTv3b because nearly identical results can be calculated from other "analyzed" datasets over the entire period (1910–2009) or "unanalyzed" datasets over the subperiod when the measurements are densely organized (e.g., after 1961).

The KE region is considered as an important center of action for PDO. Thus, we compare the KE SST variability with the PDO. The correlation between the PDOI and the MKESSTI is r=–0.65 (Fig. 3a). And the SST pattern associated with the MKESSTI also shows a PDO-like pattern, with the significant positive signals confined in the western subtropical, western and central North Pacific, and the negative signals surrounding the positive ones (Fig. 3b). These above results imply that the PDO and the KE SST variability are well related, as also suggested by Wang et al., (2012). Based on this, we further examine the wavelet spectrum of PDOI to provide another validation for the interdecadal change of KE SST variability. As we have hypothesized, similar ~6 a and ~10 a oscillations with interdecadal change are also found in the PDOI (Fig. 2), which verifies our previous finding.

Considering the profound impacts of tropical El Niño-Southern Oscillation (ENSO) on extratropical atmosphere and ocean, the relation between the ENSO and the KE SST variability is also examined. Similar to the MKESSTI, the EM of Niño-3.4 index (SST anomalies averaged in 5°S–5°N, 170°–120°W) among different datasets, which can be regarded as an objective indicator of ENSO event, is calculated and defined as the merged Niño-3.4 index (MNiño-3.4I). It can be noted that although the ENSO is well related to the PDO (i.e., r=0.43 between the MNiño-3.4I and the PDOI; Figs 3a and 5), the MKESSTI is nearly uncorrelated with the MNiño-3.4I (r=–0.13; Fig. 3a) or the tropical eastern Pacific SST signals (Fig. 3b), indicating that the KE SST variability appears to be independent with the ENSO, as also suggested by Qiu (2000).

4 Variability of the AL activity

Given the fact that the KE SST variability is closely related to the PDO, knowing the mechanism for driving the latter is expected to help understand that for driving the former. The AL variations, usually considered as the important external forcing of PDO (Schneider and Cornuelle, 2005), shows a potential linkage with the KE SST variability. Thus, the AL activity changes are investigated in detail in this section.

Following the recent work of Wang et al. (2007), three indices are defined to depict the AL activity changes: the intensity index (INTI), the east-west shift index (EWSI) and the north-south shift index (NSSI). These relatively new definitions of the AL indices need to set a searching area and a characteristic SLP contour (SLP_0). The INTI is the surface integral of difference between SLP_0 and SLP in the area surrounded by the contour SLP_0. The EWSI and NSSI represent the central position of AL. More information about these AL indices can be found in the appendix.

Figures 4a, c, e show the time series of AL indices. It can be seen that the low-frequency variability of AL is also obvious, both in its intensity and location. The SLP patterns associated with the AL intensity variation (Fig. 4b) and meridional movement (Fig.

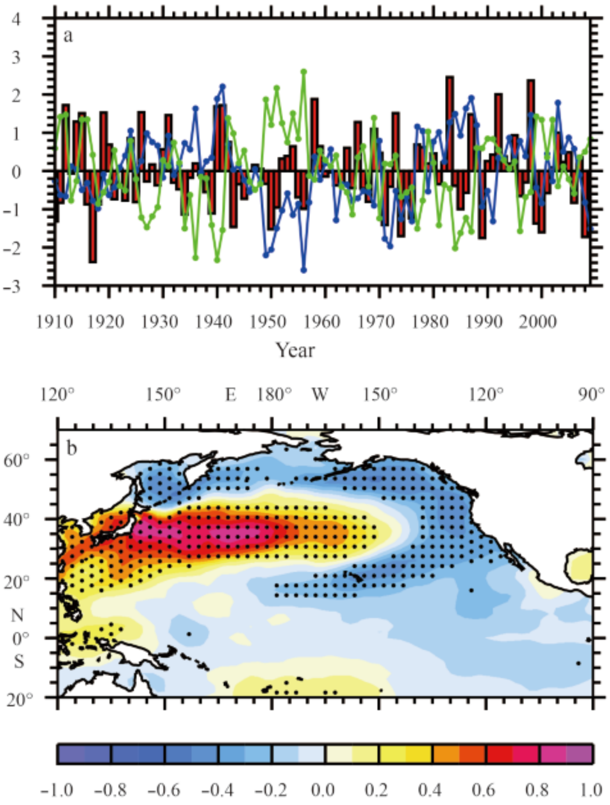

Fig. 3. Normalized time series of the merged KE SST index (MKESSTI, green line) and the merged Niño-3.4 index (MNiño-3.4I, red bars) after the removal of a linear trend, together with the PDO index (PDOI, blue line)(a), and correlation map of the MKESSTI with the SST field during 1910–2009. The stippled areas indicate where significance exceeds the 90% confidence level (b).

4f), which are nearly identical to those obtained by Sugimoto and Hanawa (1989), respectively reveal a basin-scale negative anomaly around the Aleutian Islands and a north-south dipole whose boundary locates at the latitude of about 50°N. The two patterns are totally different because the INTI is nearly uncorrelated with the NSSI (r=–0.10). However, compared with the map for the INTI, the map for the EWSI (Fig. 4d) also shows the similar negative SLP anomaly, because of the high correlation between the two time series (r=0.56).

Based on the AL indices, the relationships among the AL activity, the PDO and the ENSO are explored. As shown in Fig. 5a, the INTI is highly correlated with the PDOI (r=0.64) and its correlation map with the SST field also shows a PDO-like pattern, with the positive signals in the offshore of North America coasts

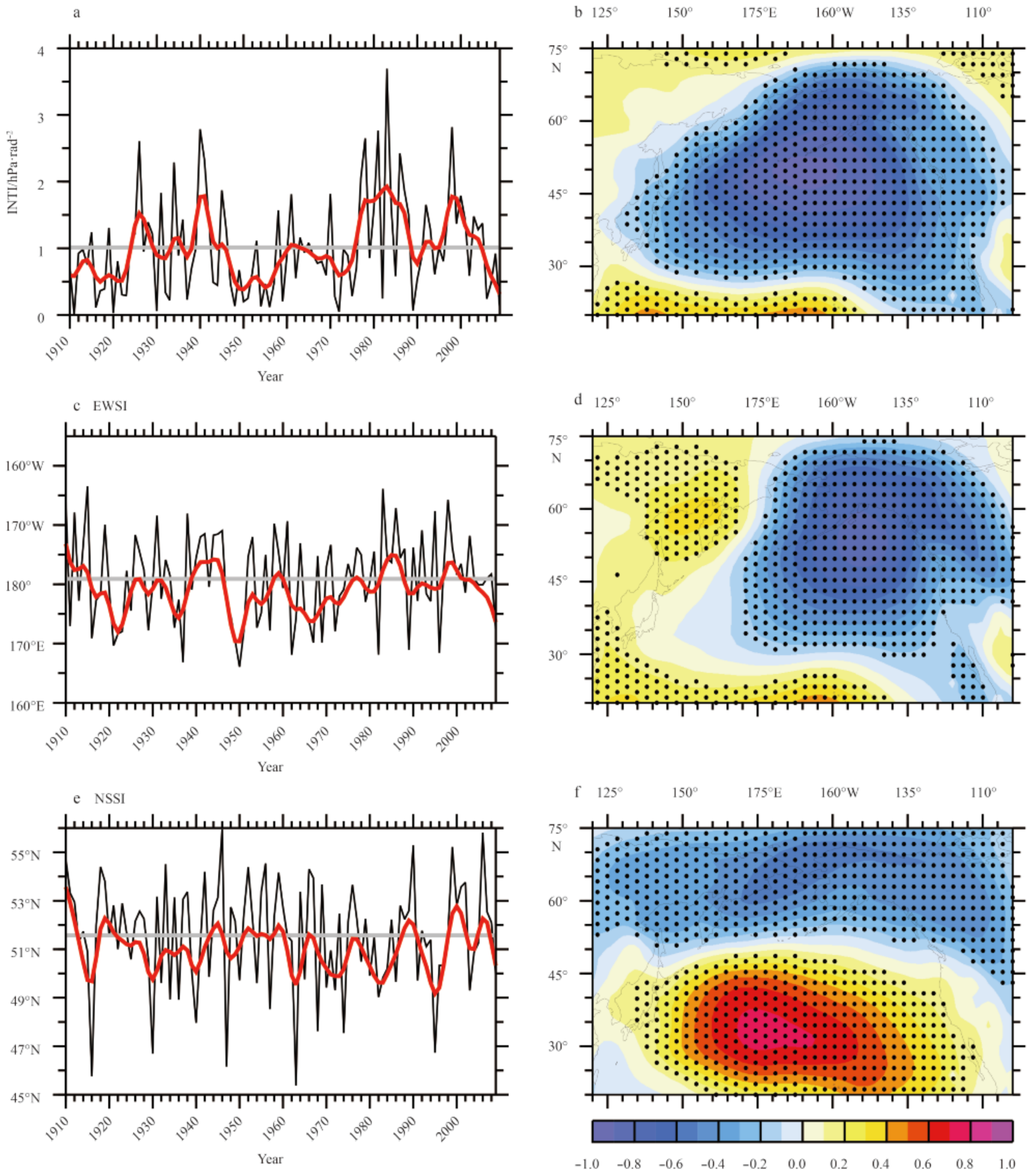

Fig. 4. The AL activity indices and their associated SLP fields. a. Time series of the intensity index (INTI). Red thick line denotes the interdecadal component (> 8 a) derived by the Gaussian filter. The horizontal gray line is the mean value for 1910–2009. b. Correlation map of the INTI with the SLP field during 1910–2009. The stippled areas indicate where significance exceeds the 90% confidence level. Figures 4 c, d, e, f as in Figs 4a, b, except for the east-west shift index (EWSI) and the north-south shift index (NSSI), respectively.

and subtropical eastern Pacific and the negative signals in the western and central North Pacific (Fig. 5c). These results reveal that the AL intensity variation is indeed well related to the PDO, as also proposed by Mantua et al. (1997). The correlation between the INTI and the MKESSTI is significant (*r*=–0.46). However, compared with the MKESSTI, the INTI is still significantly correlated with the MNiño-3.4I (*r*=0.47; Fig. 5a) or the tropical eastern Pacific SST signals (Fig. 5c). This indicates that the AL intensity variation is also related to the ENSO, consistent with the results derived by Hanawa et al. (1989) and Zhang et al. (1996). Furthermore, in consideration that the longitudinal shift of AL is concomitant with its intensity variation, as also indicated by Hanawa et al. (1989) and Overland et al. (1999), there are no additional discussions for the EWSI and its relationships with other indices or fields in the following.

Contrary to the INTI, as seen of Figs 5b and d, the NSSI is nearly uncorrelated with both the PDOI (*r*=–0.13) and the MNiño-3.4I (*r*=–0.02). The SST map associated with the NSSI also differs that associated with the INTI apparently, with the positive signals in the south and the negative signals in the north, whose nodal line is approximately at 40°N (Fig. 5d). This pattern resembles the Victoria mode indicated by Bond et al. (2003). Even though the NSSI is PDO-independent, its correlation with the MKESSTI is *r*=0.27, the value of which is relatively low but exceeds the 99% confidence level. So, the AL north-south shift is also related to the KE SST variability.

The AL activity changes are further investigated by wavelet analysis. Surprisingly, it can be seen in Fig. 6 that the KE SST-like oscillations have appeared. Specifically, the INTI and NSSI show the significant ~6 a and ~10 a oscillations during 1935–1945 and 1970–2000, respectively, indicating that the AL activity variability also exhibits the similar interdecadal change with the KE SST

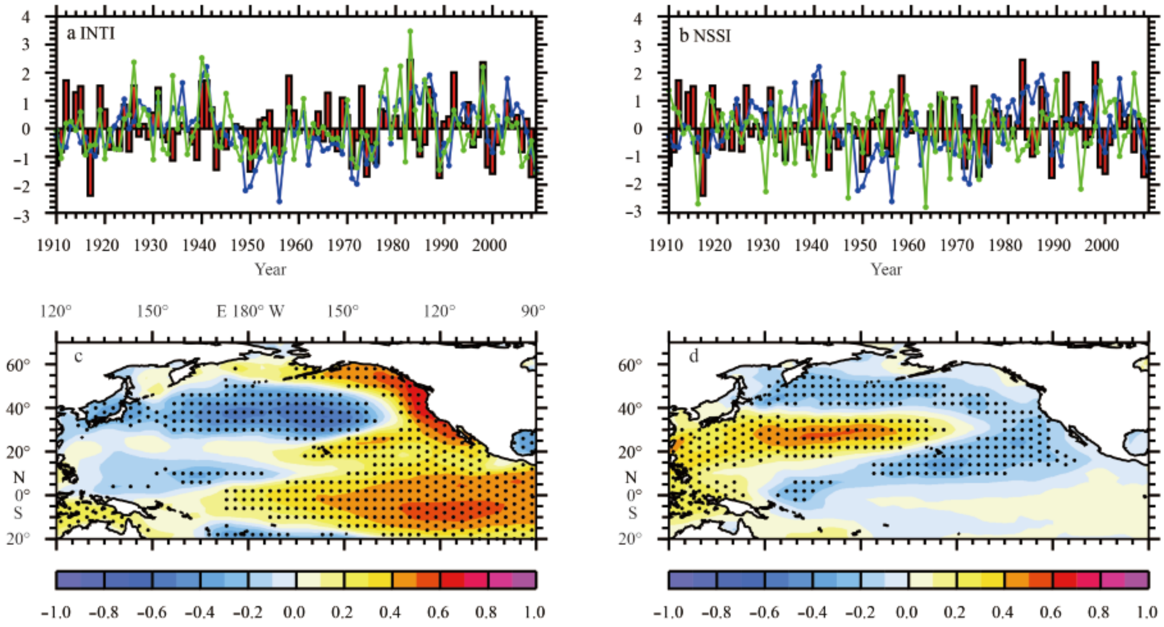

Fig. 5. Normalized time series of the INTI (green line) and the MNiño-3.4I (red bars) after the removal of a linear trend, together with the PDOI (blue line) (a), and correlation map of the INTI with the SST field during 1910–2009. The stippled areas indicate where significance exceeds the 90% confidence level (c). Figures 5b and d as in Figs 5a and c, except for the NSSI.

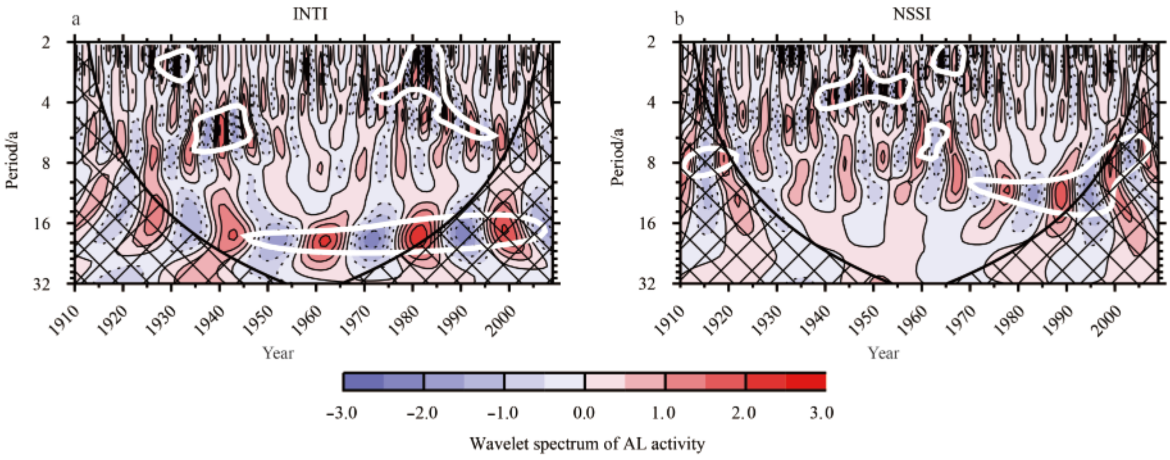

Fig. 6. Morlet wavelet transform coefficients for normalized time series of the INTI (a) and the NSSI (b). Others are the same as in Fig. 2.

variability.

5 Impacts of the AL activity on the interdecadal change of KE SST variability

The KE SST-like oscillations with interdecadal change can also be detected in the AL activity variability, indicating that the non-stationarity of KE SST variability may be related with the AL activity, which will be our focus in this section.

5.1 *Wavelet squared coherence*

A powerful tool called the wavelet squared coherence spectrum analysis can not only represent the relationship between two physical phenomena on some particular time scales but also depict its stability and variability regarding to temporal processes (Torrence and Webster, 1998). This analysis is used here to study the ~6 a and ~10 a KE SST-AL relationships. Henceforth, the word "coherence" is used to refer to the wavelet squared coherence for short.

Figure 7 (left panels) shows the coherence spectra between the MKESSTI and the AL indices. It can be seen that the time-frequency sections with high coherency correspond to those with strong signals of these indices in the wavelet spectra (Figs 2 and 6). Specifically, the KE SST variability strongly coheres with the AL intensity variation on the time scale of ~6 a during 1930–1950 (Fig. 7a) and with the AL north-south shift on the time scale of ~10 a after the 1980s (Fig. 7b). These results support that the ~6 a and ~10 a KE SST oscillations with interdecadal change are closely related with the AL activity variability.

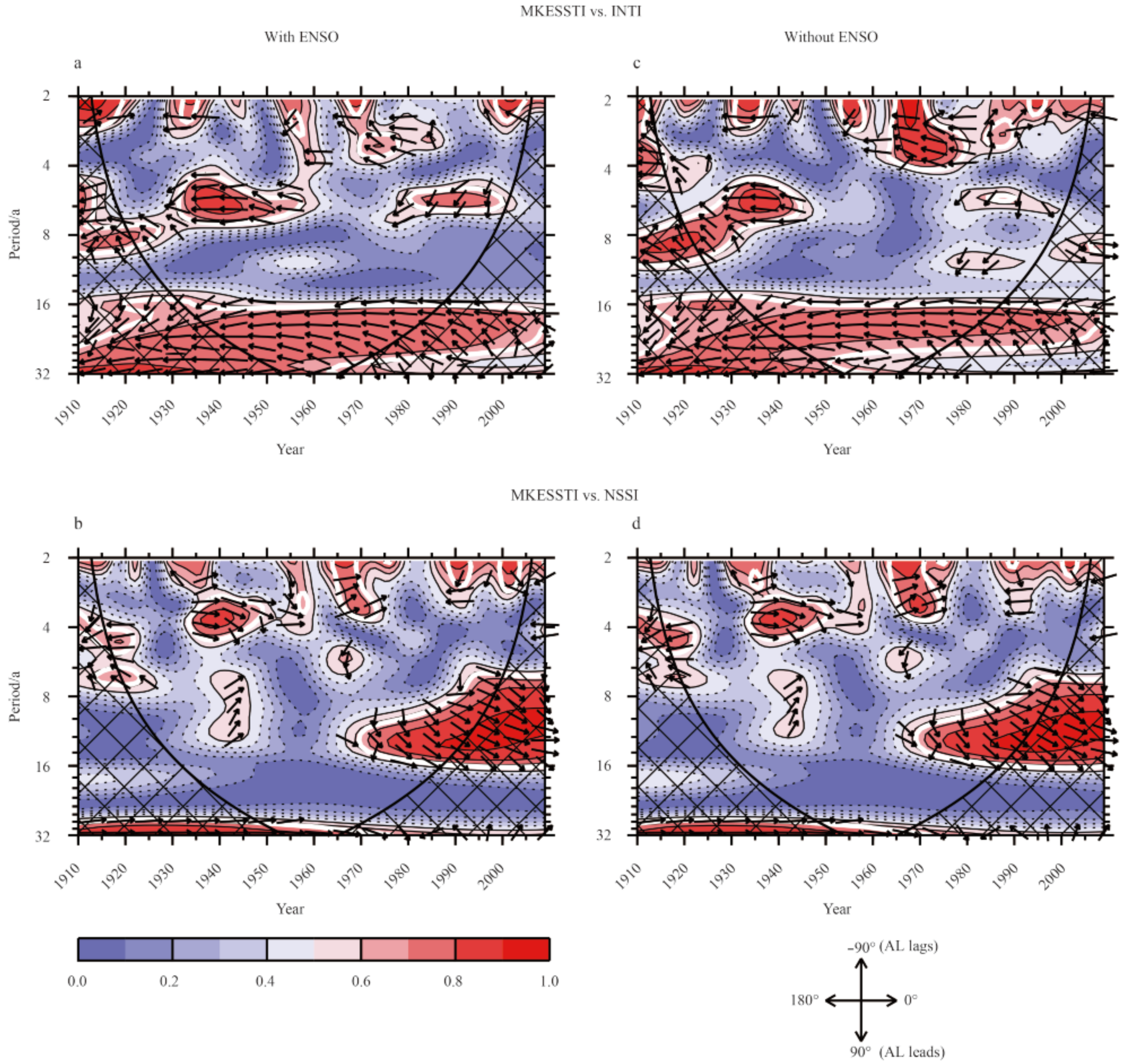

Fig. 7. Wavelet squared coherence spectra between the MKESSTI and the AL indices: the INTI (a, c) and the NSSI (b, d) corresponding to the cases with (a, b) and without (c, d) the ENSO impacts. The black vectors denote the phase difference between them (key in the lower right). For clarity, the vectors are only shown in regions with coherency > 0.5. Others are the same as in Figs 2 and 6.

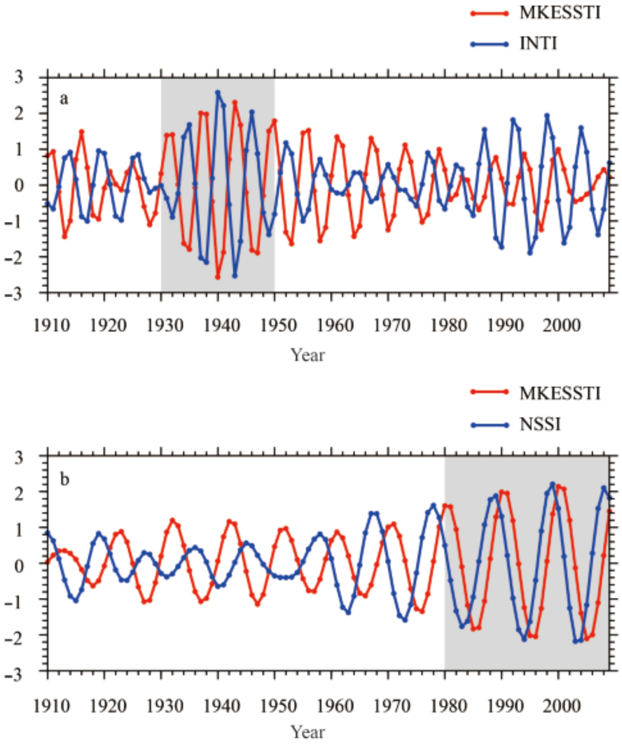

Fig. 8. Normalized time series of the ~6 a band-pass-filtered MKESSTI (red line) and INTI (blue line) after the removal of a linear trend (a). Figure 8b as in Fig. 8a, except for the ~10 a band-pass-filtered MKESSTI (red line) and NSSI (blue line). Gray shaded areas denote the two key subperiods: 1930–1950 and 1980–2009.

Another advantage of the coherence spectra is that it can be used to investigate the phase difference between the KE SST and the AL activity (Fig. 7, black vectors). To facilitate the discussion, the mean phase angles over the regions with the above-mentioned significant coherency are calculated following Grinsted et al. (2004). On the time scale of ~6 a, the MKESSTI has the mean phase angle of α=–176° with the INTI, indicating that the warm (cold) KE SST is associated with the weak (strong) AL; in other words, they are anti-correlated. On the time scale of ~10 a, the mean angle between the MKESSTI and the NSSI is α=49°, indicating that the warm (cold) KE SST lags the AL location north (south) in latitude by 1–2 years.

The similar results can also be obtained by comparing the MKESSTI and AL indices on the two time scales. To obtain the ~6 a and ~10 a time scale, the signals in the bands of 5–7 and 9–11 years are extracted by the first-order Butterworth filter. On the time scale of ~6 a, both the MKESSTI and the INTI show their maximum amplitudes during 1930–1950 when they are also better anti-correlated (r=–0.94; Fig. 8a). On the time scale of ~10 a, analogous situation occurs during 1980–2009: the amplitudes of both the MKESSTI and the NSSI are most dominant and their maximum correlation is exhibited (r=0.99) when the MKESST lags the NSSI by 2 a (Fig. 8b).

The ENSO impacts on the ~6 a and ~10 a KE SST-AL relationships are also evaluated. First, we remove the MNiño-3.4I from the MKESSTI, the INTI and the NSSI using linear regression outlined by An (2003) in the following.

The time series $\xi^*(t)$ is defined to indicate the indices including the MKESSTI, the INTI and the NSSI, and the time series $Z(t)$ is defined to denote the MNiño-3.4I. The modified time series $\xi(t)$ can be derived by filtering the signal of $Z(t)$ from $\xi^*(t)$:

$$\xi = \xi^* - Z \times \mathrm{cov}\,(\xi^*, Z)\,/\,\mathrm{var}\,(Z)\,, \tag{1}$$

where cov and var represent the covariance and variance, respectively.

After removing the ENSO influences, the coherency among the MKESSTI, the INTI and the NSSI are then re-calculated. On the time scale of ~6 a, the significant coherence between the MKESSTI and the INTI shrinks with a little shorter time span of 1930–1945 (Fig. 7c) and the mean phase angle is nearly unchanged (α=–167°). On the time scale of ~10 a, the significant coherence between the MKESSTI and the NSSI has little changes (Fig. 7d), so does its mean phase angle (α=52°). Therefore, the ENSO has the neglectable impacts on the KE SST-AL relationships on time scales of ~6 a and ~10 a.

5.2 *Possible mechanisms*

As reviewed in introduction, some authors have indicated that the ~10 a SST variability in the KE region is shaped by the incoming wind-driven Rossby waves (Kwon and Deser, 2007; Qiu et al., 2007). To detect these oceanic signals, we use the annual-mean SODA SSH field instead of the winter mean because the Rossby waves propagate year-round. Figure 9a shows a longitude-time diagram of the ~10 a band-pass-filtered SSH anomalies averaged over the meridional band of 33°–35°N, where the zonal mean KE axis is located (Seo et al., 2014), during 1980–2009. These anomalies are smoothed using the Gaussian filter with an e-folding scale of 200 km to highlight the large-scale variation. It can be seen that the Rossby waves propagate westward and reach the KE region of our interest. Based on this, the relationship between the KE SST and the Rossby waves is examined. Figure 9b shows that the MKESSTI is highly correlated with the SSH anomalies around the KE region. Between –3 a and –2 a lag, these SSH signals emerge around 170°–175°W and reach the KE region after 2–3 a, indicating that the ~10 a KE SST variability is initiated by the Rossby waves. Sugimoto and Hanawa (2009) and Seo et al. (2014) have pointed out that the atmospheric forcing of the Rossby waves is associated with the AL meridional movement. Figure 10a shows the regression map of the NSSI with the WSC field based on the ~10 a band-pass-filtered anomalies during 1980–2009. This pattern reveals that along the KE latitudinal position of about 35°N, there are large negative signals in the central North Pacific (160°–180°W) working to generate the positive SSH anomalies through the Ekman convergence. Indeed, the correlations between the NSSI and the SSH variations in the central North Pacific are generally high and reach their maximum value at 174°W (r=0.97).

As described above, on the time scale of ~10 a, the AL north-south shift impacts the KE SST variability via inducing the Rossby waves. However, can the ~6 a KE SST variability also be explained by Rossby wave dynamics? We infer this may not be possible because the basin-crossing time of Rossby waves usually tends to select a decadal time scale (Kwon and Deser, 2007; Qiu et al., 2007). Indeed, on the time scale of ~6 a, it is found that the SSH anomalies propagate eastward in the KE region (Fig. 9c), indicating that there are no incoming Rossby waves. Comparing Fig. 9d with Fig. 9b, the MKESSTI is also positively correlated with the SSH signals around the KE region, but the latter is not caused by the Rossby waves formed in the central North Pacific because the negative correlations are shown therein when the

MKESSTI lags by 2–3 years. From the atmospheric aspect, although the AL intensity variation can excite the WSC anomalies working to induce the Rossby waves in the central North Pacific as well (Fig. 10b), the delayed ocean adjustment, which is attributable to the Rossby wave propagation, is not able to account for that the maximum correlation between the INTI and the MKESSTI occurs simultaneously. Therefore, the AL activity can not impact the KE SST variability through the bridge of Rossby

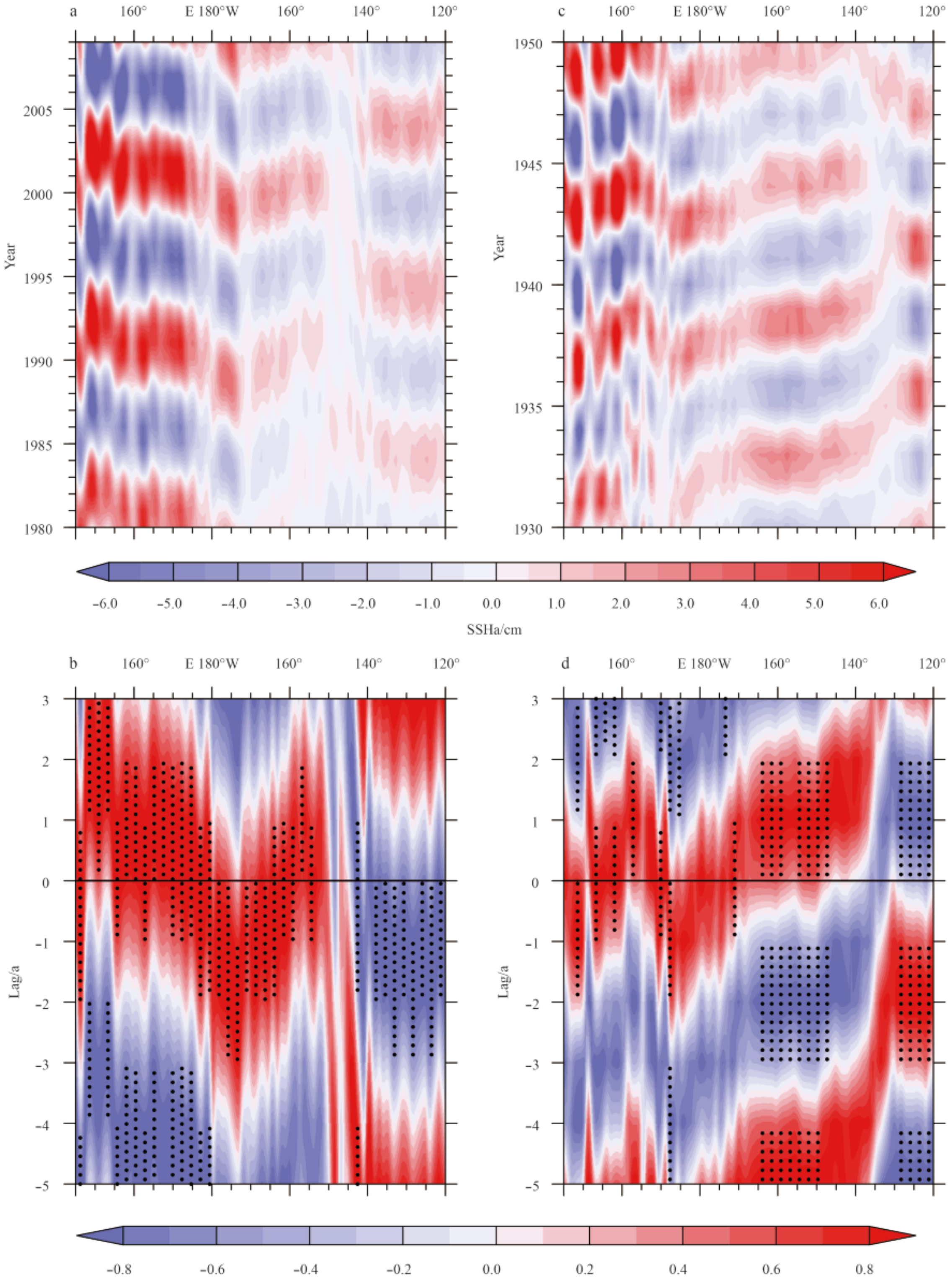

Fig. 9. Hovmöller diagram of the ~10 a band-pass-filtered annual mean SSH anomalies averaged within the latitudinal band of 33°–35°N during 1980–2009 (a), and lag-longitude correlation diagram of the MKESSTI in Fig. 8b (red line) with the SSH anomalies in Fig. 9a (b). Positive lags mean that the MKESSTI has lead lags. The stippled areas indicate where significance exceeds the 90% confidence level. Figure 9c as in FIg. 9a, except for the ~6 a band-pass-filtered annual mean SSH anomalies during 1930–1950. Figure 9d as in Fig. 9b, except for the MKESSTI in Fig. 8a (red line) and the SSH anomalies in Fig. 9c.

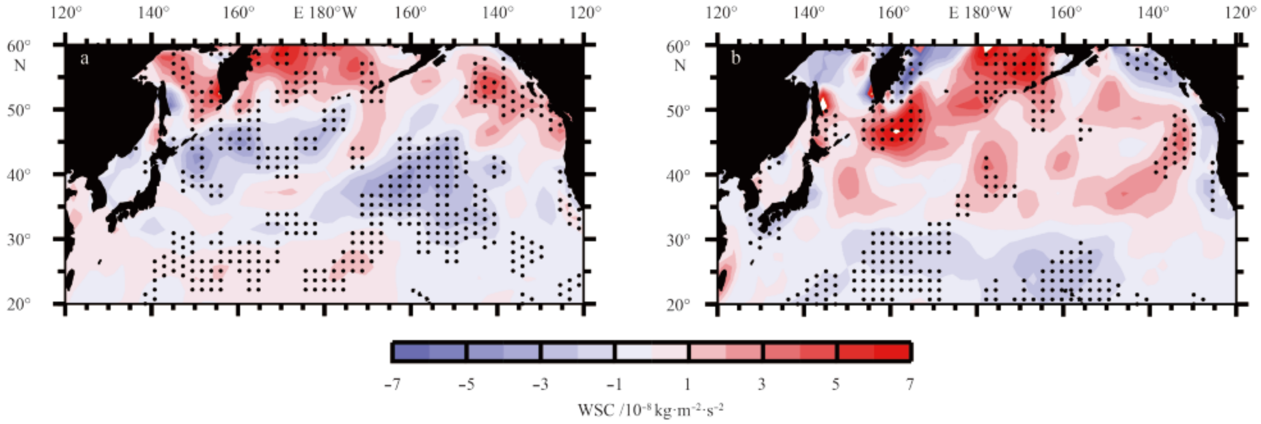

Fig. 10. Regression map of the NSSI with the wind stress curl (WSC) field based on the ~10 a band-pass-filtered anomalies during 1980–2009 (a). Figure 10b as in Fig. 10a, except for the ~6 a band-pass-filtered INTI and WSC field during 1930–1950. The stippled areas indicate where significance exceeds the 90% confidence level.

waves in the central North Pacific on the time scale of ~6 a.

Miller et al. (1994) have suggested that the AL intensity variation can also impact the underlying KE SST via altering the air-sea heat flux exchange, Ekman advection and wind-induced vertical mixing. To test whether this is true on the time scale of ~6 a during 1930–1950, the two former leading processes are emphasized and examined by using a simplified mixed layer heat budget equation (Ciasto and England, 2011):

$$\rho C_{\rm p} h \frac{\partial SST}{\partial t} = Q_{\rm net} + Q_{\rm Ek} + R, \qquad (2)$$

where, ρ is the density of seawater, $C_{\rm p}$ is the heat capacity of seawater, h is the mixed layer depth, $Q_{\rm net}$ is the net surface heat flux (i.e., the sum of radiative and turbulent heat fluxes), $Q_{\rm Ek}$ is the Ekman heat flux (i.e., the advection of SST driven by wind-induced Ekman currents) and is related to wind stress vector τ, SST and Coliolis parameter f by $Q_{\rm Ek}=-[C_{\rm p}(\tau\times {\rm k})\cdot SST]/f$, R is the residual including all terms not listed (i.e., diffusion, vertical convection, and geostrophic heat flux).

The $Q_{\rm net}$ and $Q_{\rm Ek}$ fields are simultaneously regressed on the INTI. It is found that the net surface heat flux forcing tends to generate the cold SST anomalies in the western North Pacific but the warm ones in the eastern North Pacific (Fig. 11a), while the Ekman heat flux forcing contributes to cool the SST in the whole North Pacific basin (Fig. 11b). However, both of the net surface and Ekman heat fluxes can cause the cold SST anomalies in the KE region. The pattern for the sum of $Q_{\rm net}$ and $Q_{\rm Ek}$ (Fig. 11c) shows large negative anomalies in the western subtropical, western and central North Pacific but positive anomalies along the

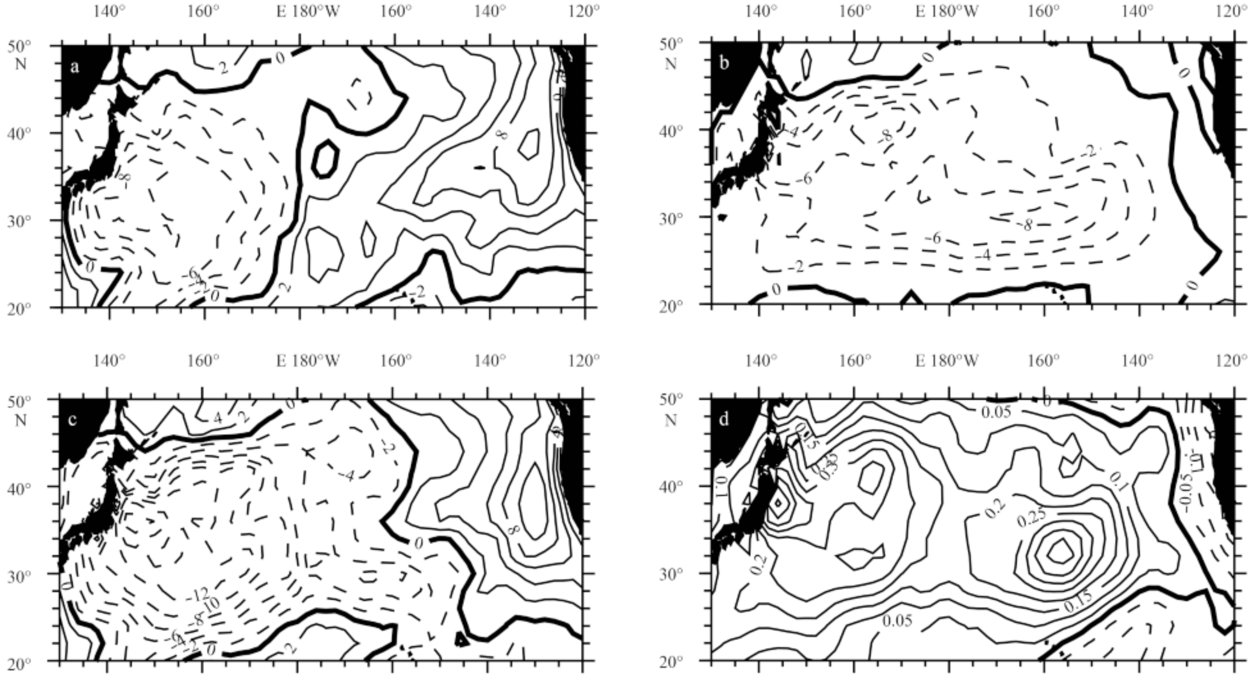

Fig. 11. Regression map of the INTI with the fields of net surface heat flux (a) and Ekman heat flux based on the ~6 a band-pass-filtered anomalies during 1930–1950 (b). Figure 11c is the sum of Figs 11a and b. Figure 11d as in Figs 11a and b, except for the MKESSTI and the SST field. Units are W/m² for the heat flux and °C for the SST.

North America coast. This pattern is very similar with that for the MKESSTI-related SST anomalies with the opposite signs (Fig. 11d). The pattern correlation between Fig. 11c and Fig. 11d is *r*=–0.73, the value of which exceeds the 99% confidence level, indicating that the anomalous net surface and Ekman heat fluxes related to the AL intensity variation can reproduce the KE SST anomalies fairly well on the time scale of ~6 a. Furthermore, decomposition of the Ekman heat flux into $-\left[C_{\mathrm{p}}\left(\tau'_{\mathrm{INTI}}\times k\right)\cdot\nabla\overline{SST}\right]/f$, $-\left[C_{\mathrm{p}}\left(\bar{\tau}\times k\right)\cdot\nabla SST'_{\mathrm{INTI}}\right]/f$, and $-\left[C_{\mathrm{p}}\left(\tau'_{\mathrm{INTI}}\times k\right)\cdot\nabla SST'_{\mathrm{INTI}}\right]/f$, where the term with a overbar denotes its JFM mean and the term with a prime and a subscript denotes its anomaly from the JFM mean regressed on the INTI. The result reveals that the total Ekman heat flux is largely determined by the anomalous wind stress associated with the INTI and the gradient of the mean SST (not shown). This indicates a direct forcing of the KE SST anomalies by the AL-induced Ekman heat transport.

Based on Eq. (1), we also investigate that whether the AL north-south shift is able to impact the ~10 a KE SST variability 2 years later via affecting the two terms (Q_{net} and Q_{Ek}) during 1980–2009. It is found that the north location of AL leads to the negative net surface heat flux anomalies working to cool the SST in the KE region (Fig. 12a). Although the relevant Ekman heat flux forcing contributes to warm the KE SST, this effect has a lower magnitude in average and is damped by the net surface heat flux forcing (Fig. 12b). Therefore, the sum of Q_{net} and Q_{Ek} forcing acts to generate the cold SST anomalies in most of the KE region (Fig. 12c), which is at odds with the fact that the AL location in north causes the warm KE SST two years later as elucidated before. Moreover, the sum of the two terms also fails to reconstruct the SST pattern associated with the MKESSTI (Fig. 12d) because their pattern correlation is only *r*=0.30. Combined with the results analyzed previously, these diagnoses confirm that the AL north-south shift mainly determines the ~10 a KE SST variability by inducing the oceanic Rossby waves, rather than the anomalous surface heat flux forcing and Ekman heat transport.

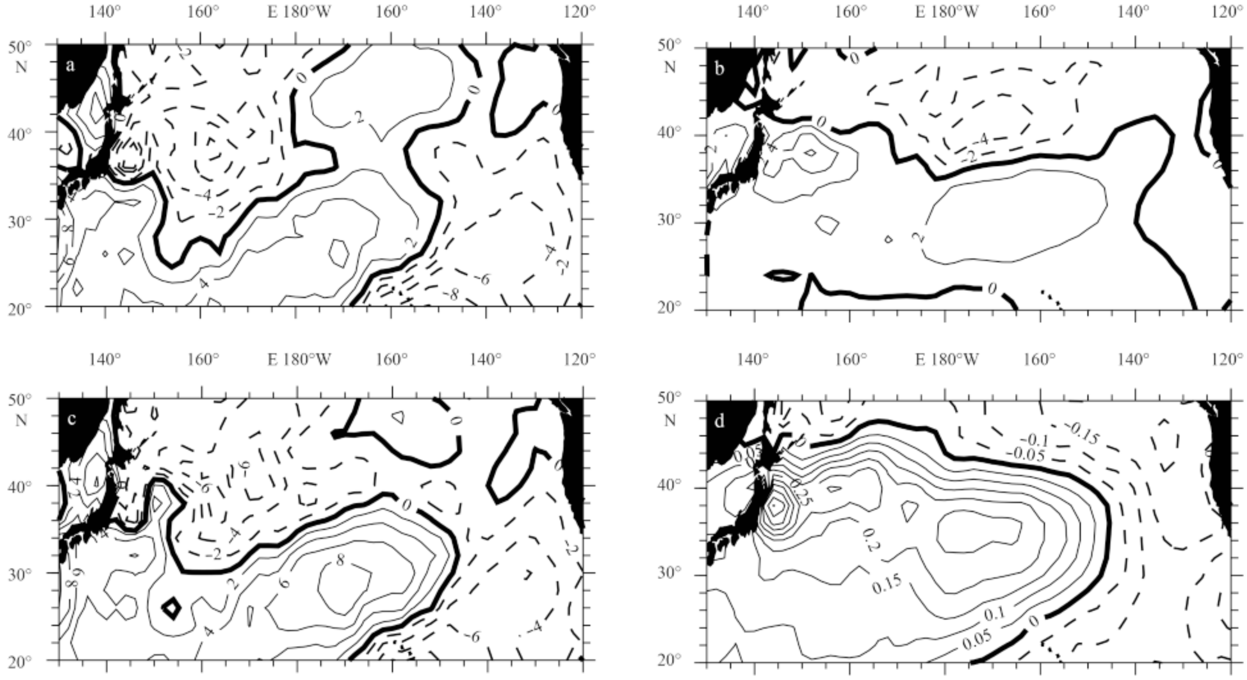

Fig. 12. Same as in Fig. 11, except for regression map of the NSSI with the fields of net surface heat flux (a) and Ekman heat flux when the NSSI leads by 2 a based on the ~10 a band-pass-filtered anomalies during 1980–2009 (b). Figure 12c is the sum of Figs 12a and b. Figure 12d as in Figs 12a and b, except for the simultaneous regression between the MKESSTI and the SST field.

6 Conclusions

By using multiple datasets from various sources available for the last 100 years, the existence for the interdecadal change of winter SST variability in the KE region is investigated. And its linkage with the AL activity changes is also discussed.

The KE SST variability exhibits significant ~6 a and ~10 a oscillations with obvious interdecadal change: the ~6 a oscillation with large amplitudes is mainly detected during 1930–1950; however, it becomes weaker with time and is gradually overtaken by the ~10 a one after the 1980s. The consistency among different datasets verifies that it is robust for this phenomenon.

The AL activity variability also exhibits the similar interdecadal change: the AL intensity variation and north-south shift show the significant ~6 a and ~10 a oscillations during 1935–1945 and 1970–2000, respectively. This contributes to the non-stationarity of the KE SST variability. During 1930–1950, the AL intensity variation is the main impact factor of the ~6 a KE SST variability via causing anomalous surface heat flux forcing and Ekman heat transport. However, after the 1980s, the oceanic Rossby waves induced by the AL north-south shift play the dominant role in triggering the ~10 a KE SST variability. The timing of change in the KE SST variability nearly accords with the climate transition in the late 1970s in the North Pacific. It is implied that the climate regime shift is important in modulating the KE SST variability, which also needs to be explored in further studies.

References

An S I. 2003. Conditional maximum covariance analysis and its application to the tropical Indian Ocean SST and surface wind stress anomalies. J Climate, 16(17): 2932–2938

Bond N A, Overland J E, Spillane M, et al. 2003. Recent shifts in the state of the North Pacific. Geophys Res Lett, 30(23): 2183, doi: 10.1029/2003GL018597

Bretherton C S, Widman M, Dymnikov V P, et al. 1999. The effective number of spatial degrees of freedom of a time-varying field. J Climate, 12(7): 1990–2009

Brohan P, Kennedy J J, Harris I, et al. 2006. Uncertainty estimates in regional and global observed temperature changes: A new data set from 1850. J Geosphys Res, 111(D12): D12106, doi: 10.1029/2005JD006548

Carton J A, Giese B S. 2008. A reanalysis of ocean climate using Simple Ocean Data Assimilation (SODA). Mon Wea Rev, 136(8): 2999–3017

Ciasto L M, England M H. 2011. Observed ENSO teleconnections to Southern Ocean SST anomalies diagnosed from a surface mixed layer heat budget. Geophys Res Lett, 38(9): L09701, doi: 10.1029/2011GL046895

Compo G P, Whitaker J S, Sardeshmukh P D, et al. 2011. The twentieth century reanalysis project. Quart J Roy Meteor Soc, 137(654): 1–28

Deser C, Phillips A S. 2006. Simulation of the 1976/77 climate transition over the North Pacific: Sensitivity to tropical forcing. J Climate, 19(23): 6170–6180

Deser C, Phillips A S, Alexander M A. 2010. Twentieth century tropical sea surface temperature trends revisited. Geophys Res Lett, 37(10): L10701, doi: 10.1029/2010GL043321

Ding Ruiqiang, Li Jianping, Tseng Y H, et al. 2015. The Victoria mode in the North Pacific linking extratropical sea level pressure variations to ENSO. J Geophys Res, 120(1): 27–45

Giese B S, Ray S. 2011. El Niño variability in simple ocean data assimilation (SODA), 1871–2008. J Geophys Res, 116(C2): C02024, doi: 10.1029/2010JC006695

Graham N E. 1994. Decadal scale climate variability in the tropical and North Pacific during the 1970s and 1980s: Observations and model results. Climate Dyn, 10(3): 135–162

Grinsted A, Moore J C, Jevrejeva S. 2004. Application of the cross wavelet transform and wavelet coherence to geophysical time series. Nonlinear Processes in Geophysics, 11(5–6): 561–566

Hanawa K, Yoshikawa Y, Watanabe T. 1989. Composite analyses of wintertime wind stress vector fields with respect to SST anomalies in the western North Pacific and the ENSO events: Part II. ENSO composite. J Meteor Soc Japan, 67(5): 835–845

Ishi Y, Hanawa K. 2005. Large-scale variabilities of wintertime wind stress curl field in the North Pacific and their relation to atmospheric teleconnection patterns. Geophys Res Lett, 32(10): L10607, doi: 10.1029/2004GL022330

Jin Qihua, Wang Hui. 2011. Multitime scale variations of sea surface temperature in the China seas based on the HadISST dataset. Acta Oceanologica Sinica, 30(4): 14–23

Kaplan A, Cane M A, Kushnir Y, et al. 1998. Analyses of global sea surface temperature 1856–1991. J Geophys Res, 103(C9): 18567–18589

Kelly K A, Small R J, Samelson R M, et al. 2010. Western boundary currents and frontal air–sea interaction: Gulf Stream and Kuroshio Extension. J Climate, 23(21): 5644–5667

Kennedy J J, Rayner N A, Smith R O, et al. 2011a. Reassessing biases and other uncertainties in sea surface temperature observations measured in situ since 1850: 1. Measurement and sampling uncertainties. J Geophys Res, 116(D14): D14103, doi: 10.1029/2010JD015218

Kennedy J J, Rayner N A, Smith R O, et al. 2011b. Reassessing biases and other uncertainties in sea surface temperature observations measured in situ since 1850: 2. Biases and homogenization. J Geophys Res, 116(D14): D14104, doi: 10.1029/2010JD015220

Kwon Y O, Deser C. 2007. North Pacific decadal variability in the Community Climate System Model version 2. J Climate, 20(11): 2416–2433

Latif M, Barnett T P. 1994. Causes of decadal climate variability over the North Pacific and North America. Science, 266(5185): 634–637

Latif M, Barnett T P. 1996. Decadal climate variability over the North Pacific and North America: Dynamics and predictability. J Climate, 9(10): 2407–2423

Li Jianping, Sun Cheng, Jin Feifei. 2013. NAO implicated as a predictor of Northern Hemisphere mean temperature multidecadal variability. Geophys Res Lett, 40(20): 5497–5502

Liu Qinyu, Wen Na, Yu Yongqiang. 2006. The role of the Kuroshio in the winter North Pacific ocean-atmospheric interaction: comparison of a coupled model and observations. Adv Atmos Sci, 23(2): 181–189

Mantua N J, Hare S R, Zhang Yuan, et al. 1997. A Pacific interdecadal climate oscillation with impacts on salmon production. Bull Amer Meteor Soc, 78(6): 1069–1079

Miller A J, Cayan D R, Barnett T P, et al. 1994. The 1976–77 climate shift of the Pacific Ocean. Oceanography, 7(1): 21–26

Minobe S, Maeda A. 2005. A 1° monthly gridded sea-surface temperature dataset compiled from ICOADS from 1850 to 2002 and Northern Hemisphere frontal variability. Int J Climatol, 25(7): 881–994

Overland J E, Adams J M, Bond N A. 1999. Decadal variability of the Aleutian Low and its relation to high-latitude circulation. J Climate, 12(5): 1542–1548

Peng Shiling, Whitaker J S. 1999. Mechanisms determining the atmospheric response to midlatitude SST anomalies. J Climate, 12(5): 1393–1408

Qiu Bo. 2000. Interannual variability of the Kuroshio Extension system and its impact on the wintertime SST field. J Phys Oceanogr, 30(6): 1486–1502

Qiu Bo. 2003. Kuroshio Extension variability and forcing of the Pacific decadal oscillations: Responses and potential feedback. J Phys Oceanogr, 33(12): 2465–2482

Qiu Bo, Chen Shuiming. 2005. Variability of the Kuroshio Extension jet, recirculation gyre, and mesoscale eddies on decadal time scales. J Phys Oceanogr, 35(11): 2090–2103

Qiu Bo, Chen Shuiming. 2010. Eddy-mean flow interaction in the decadally modulating Kuroshio Extension system. Deep Sea Research, 57(13–14): 1098–1110

Qiu Bo, Schneider N, Chen Shuiming. 2007. Coupled decadal variability in the North Pacific: An observationally constrained idealized model. J Climate, 20(14): 3602–3620

Rayner N A, Brohan P, Parker D E, et al. 2006. Improved analyses of changes and uncertainties in sea surface temperature measured in situ since the mid-nineteenth century: The HadSST2 dataset. J Climate, 19(3): 446–469

Rayner N A, Parker D E, Horton E B, et al. 2003. Global analyses of sea surface temperature, sea ice, and night marine air temperature since the late nineteenth century. Journal of Geophysical Research, 108(D14): 4407, doi: 10.1029/2002JD002670

Schneider N, Cornuelle B D. 2005. The forcing of the Pacific decadal oscillation. J Climate, 18(21): 4355–4373

Seo Y, Sugimoto S, Hanawa K. 2014. Long-term variations of the Kuroshio Extension path in winter: Meridional movement and path state change. J Climate, 27(15): 5929–5940

Smith T M, Reynolds R W, Peterson T C, et al. 2008. Improvements to NOAA's historical merged land-ocean surface temperature analysis (1880–2006). J Climate, 21(10): 2283–2296

Sugimoto S, Hanawa K. 2009. Decadal and interdecadal variations of the Aleutian low activity and their relation to upper oceanic variations over the North Pacific. J Meteor Soc Japan, 87(4): 601–614

Tanimoto Y, Nakamura H, Kagimoto T, et al. 2003. An active role of extratropical sea surface temperature anomalies in determining anomalous turbulent heat flux. J Geophys Resh, 108(C10): 3304, doi: 10.1029/2002JC001750

Torrence C, Compo G P. 1998. A practical guide to wavelet analysis. Bull Amer Meteor Soc, 79(1): 61–78

Trenberth K E. 1984. Some effects of finite sample size and persistence on meteorological statistics. Part I: autocorrelations. Mon Wea Rev, 112(12): 2359–2368

Trenberth K E. Hurrell J W. 1994. Decadal atmosphere–ocean variations in the Pacific. Climate Dyn, 9(6): 303–319

Trenberth K E. 1990. Recent observed interdecadal climate changes in the Northern Hemisphere. Bull Amer Meteor Soc, 71(7): 988–993

Vivier F, Kelly E A, Thompson L. 2002. Heat budget in the Kuroshio Extension region: 1993–1999. J Phys Oceanogr, 32(12): 3436–3454

Wang Shanshan, Guan Yuping, Li Zhijin, et al. 2012. Preliminary analyses on characteristics of sea surface temperatures in Kuroshio and its extension and relations to atmospheric circulations. Acta Physica Sinica (in Chinese), 61(16): 169201

Wang Shanshan, Guan Yuping, Li Zhijin, et al. 2015. Variable characteristics of the wintertime net heat flux along the Kuroshio system and its association with climate in China. Int J Climatol, 35(6): 1180–1191

Wang Panxing, Lu Chuhan, Guan Zhaoyong, et al. 2007. Definition and calculation of three circulation indices for closed pressure systems. Journal of Nanjing Institute of Meteorology (in Chinese), 30(6): 730–735.

Wu Lixin, Cai Wenju, Zhang Liping, et al. 2012. Enhanced warming over the global subtropical western boundary currents. Nature Climate Change, 2(3): 161–166

Zhang Jinting, Liu Qinyu, Wu Shu. 2010. The analysis of interannual and interdecadal characteristics of global sea surface temperature during 1902–2003. Haiyang Xuebao (in Chinese), 32(4): 24–31

Zhang Yuan, Wallace J M, Iwasaka N. 1996. Is climate variability over the North Pacific a linear response to ENSO?. J Climate, 9(7): 1468–1478

Appendix

Next, we introduce how to define and calculate the AL index used in this paper, which facilitates the investigation for the AL activity changes in details.

Three indices to depict the in situ magnitude and location changes of AL: the intensity index (INTI), the east-west index (EWSI), and the north-south index (NSSI) are defined. The INTI has the following form:

$$INTI = -\iint_D \left(\mathrm{SLP}\,(\lambda,\theta) - \mathrm{SLP}_0\right)\mathrm{d}s = \iint_D \Delta P\,(\lambda,\theta)\,\mathrm{d}s, \tag{A1}$$

where *D* is the area surrounded by the characteristic SLP contour (SLP_0). d*s* denotes the infinitesimal area occupied by a grid point. and represent the longitude and latitude of a SLP grid point, respectively. Eq. (A1) actually indicates the surface integral of the difference between SLP_0 and SLP (*P*) in the *D*.

To find the central position of AL, a coordinate system *oxy* with the origin point of North Pole and axes along with the meridian of 0° and 90°E is built (Fig. A1a). The (,) can be transformed into (*x*, *y*) coordinates in *oxy* according to the spherical geometric relations as follows:

$$x = \arctan\left(\tan\left(\frac{\pi}{2} - \theta\right)\cos\lambda\right), \tag{A2}$$

$$y = \arctan\left(\tan\left(\frac{\pi}{2} - \theta\right)\sin\lambda\right), \tag{A3}$$

based on Eq. (A2) and (A3), we can obtain the (*x*, *y*) of all SLP grid points in the area of our focus, then the location of AL center can be defined,

$$x_c = \left[\iint_D x\,(\lambda,\theta)\,\Delta P\,(\lambda,\theta)\,ds\right] / INTI, \tag{A4}$$

$$y_c = \left[\iint_D y\,(\lambda,\theta)\,\Delta P\,(\lambda,\theta)\,ds\right] / INTI, \tag{A5}$$

Equations (A4) and (A5) represent the location of *P* centroid. The EWSI and NSSI are calculated by inverse transforming the (x_c, y_c) into ($_c$, $_c$) through:

$$EWSI = \lambda_c = \arctan\left(\tan\, y_c / \tan\, x_c\right), \tag{A6}$$

$$NSSI = \theta_c = \frac{\pi}{2} - \arctan\left(\tan^2\, x_c + \tan^2\, y_c\right)^{-1/2}. \tag{A7}$$

Even though the processes for determining these AL indices are clear, we must confirm the SLP_0 and the searching area Ω only in which the SLP of grid points is compared with the SLP_0 for calculation. The 1 008 hPa is chosen to be the SLP_0. The reasons conclude the two aspects: (1) the 1 008 hPa contour can indicate the AL and separate it from the polar vortex system well (Fig. A1b, gray contours); (2) the 1 008 hPa is a critical value which can always guarantee that the SLP of some grid points in the Ω is lower than it in each year from 1910 to 2009 so that all the AL indices in the time domain of our interest are obtained successfully. We also find the AL activity range indicated by the SLP_0 is restricted in the region of 32°–70°N, 140°E–124°W for the last 100 years (Fig. A1b, red dashed line), which is defined as the Ω.

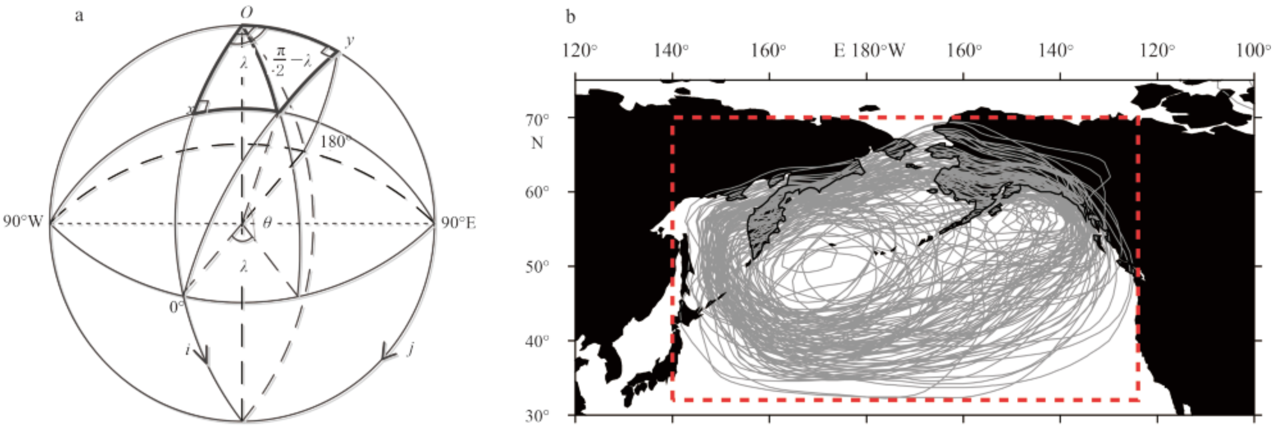

Fig. A1. Coordinate system *oxy* on the spherical surface of a unit radius. (Adapted from Wang et al., 2007)(a), and spatial distribution of the 1 008 hPa contour indicating the characteristic SLP contour of AL from 1910 to 2009 (gray contours), and rectangle (red dashed line) denotes the searching area (b).